



This is a repository copy of *Comparison of BSPT and PZT piezoelectric ceramic transformers for high temperature power supplies.*

White Rose Research Online URL for this paper:

<https://eprints.whiterose.ac.uk/189891/>

Version: Published Version

Article:

Forrester, J. orcid.org/0000-0002-8102-7576, Li, L., Yang, Z. et al. (5 more authors) (2022) Comparison of BSPT and PZT piezoelectric ceramic transformers for high temperature power supplies. *Advanced Engineering Materials*, 24 (12). 2200513. ISSN 1438-1656

<https://doi.org/10.1002/adem.202200513>

Reuse

This article is distributed under the terms of the Creative Commons Attribution (CC BY) licence. This licence allows you to distribute, remix, tweak, and build upon the work, even commercially, as long as you credit the authors for the original work. More information and the full terms of the licence here:

<https://creativecommons.org/licenses/>

Takedown

If you consider content in White Rose Research Online to be in breach of UK law, please notify us by emailing eprints@whiterose.ac.uk including the URL of the record and the reason for the withdrawal request.



eprints@whiterose.ac.uk
<https://eprints.whiterose.ac.uk/>

Comparison of BSPT and PZT Piezoelectric Ceramic Transformers for High-Temperature Power Supplies

Jack Forrester,* Linhao Li, Zijiang Yang, Jonathan N. Davidson, Derek C. Sinclair, Ian M. Reaney, Martin P. Foster, and David A. Stone

High-temperature power electronics is an advancing area of research, especially given the widespread availability of wide bandgap semiconductors. Herein, a suitability analysis of $(1-x)\text{BiScO}_3-x\text{PbTiO}_3$ (BSPT) as a material for high-temperature piezoelectric transformers (PTs) is presented and compared to state-of-the-art $\text{Pb}(\text{Zr}_{1-x}\text{Ti}_x)\text{O}_3$ (PZT). Initially, both materials are compared using a variety of metrics to prove the suitability of BSPT as a material for constructing PTs specifically for high-temperature applications. PTs based on the two materials are designed and fabricated, and then subsequently characterized using impedance measurements. Finally, half-bridge resonant inverters are constructed using both PTs and the performance of each inverter measured over a range of ambient temperatures. The result of these experiments confirms the suitability of BSPT for PT applications and shows the excellent performance of BSPT PTs at temperatures in excess of that possible with PZT-based PTs.

field is generated across the sensor (output). PTs have several advantages over their magnetic counterparts including high power density and high efficiency. They are also free from stray electromagnetic fields and related emission and sensitivity problems.^[4–6] PTs can also adopt various structural shapes, operating modes, voltage ratios, and operating frequencies, allowing them to fulfill a range of design requirements.

Wide bandgap semiconductor materials and devices (i.e., SiC and GaN) are now achieving commercial success since their higher operating frequency and lower losses translate to a reduction in passive component size and thereby an increase in power density.^[7] Wide bandgap devices can also operate at higher temperatures

than Si-based devices and so engineers are investigating the opportunities this makes available, but are restricted due to the lack of high temperature capable passive components.^[8,9]

There are several potential applications of high-temperature power converters such as downhole (oil and geothermal wells) for power logging and monitoring tools at temperatures of up to 250 and 350 °C, respectively. In electric and conventional vehicles, they can be used for powering the motors and sensors at up to 300 °C. In the aerospace industry, they can be used for the control circuitry, motor and braking controls, and for simplifying the electrical design at temperatures of up to 350 °C.^[10,11]

$\text{Pb}(\text{Zr}_{1-x}\text{Ti}_x)\text{O}_3$ (PZT)-based ceramics have been the most successful piezoelectrics since their development in the 1950s.^[1,12–14] The most common PZT ceramics lie near the morphotropic phase boundary (MPB), between tetragonal (PbTiO_3) and rhombohedral (PbZrO_3) phases, where PZT exhibits anomalously high dielectric and piezoelectric properties. These exceptional properties have driven a wide range of applications such that PZT is ubiquitous throughout modern life. However, depending on the application, PZT-based bulk ceramics are limited in their operating temperature to $\approx 50\text{--}100$ °C below their Curie temperature ($T_C = 386$ °C for undoped MPB PZT), which means a realistic upper temperature of operation for PZT-based devices is around 200 °C.^[15]

In 2001, Eitel et al. reported a ceramic solid solution system $(1-x)\text{BiScO}_3-x\text{PbTiO}_3$ (BSPT) with an MPB around $x = 0.64$ between the tetragonal (PbTiO_3) and rhombohedral (BiScO_3) phase regions.^[16–19] Compared to PZT, BSPT ceramics have a lower concentration of PbO, a comparable piezoelectric constant,

1. Introduction

Piezoelectric materials experience mechanical deformations when placed in an electric field and become electrically polarized under applied mechanical stress. A range of electromechanical devices can be designed based on these two effects including transducers, sensors, and actuators.^[1–3] By bonding a piezoelectric actuator to a piezoelectric transducer, an energy transformation device is created that is similar in behavior to an electromagnetic transformer. This device is known as a piezoelectric transformer (PT). The transducer (the input) is driven to produce vibration, which due to the mechanical bonding causes the sensor to vibrate, thus a proportional electric

J. Forrester, Z. Yang, J. N. Davidson, M. P. Foster, D. A. Stone
Electronic and Electrical Engineering
University of Sheffield
Sheffield S1 3JD, UK
E-mail: jack.forrester@sheffield.ac.uk

L. Li, D. C. Sinclair, I. M. Reaney
Materials Science and Engineering
University of Sheffield
Sheffield S1 3JD, UK

 The ORCID identification number(s) for the author(s) of this article can be found under <https://doi.org/10.1002/adem.202200513>.

© 2022 The Authors. Advanced Engineering Materials published by Wiley-VCH GmbH. This is an open access article under the terms of the Creative Commons Attribution License, which permits use, distribution and reproduction in any medium, provided the original work is properly cited.

DOI: 10.1002/adem.202200513

$d_{33} = 450$ pC/N, and electromechanical coupling factor, $k_p = 0.58$, but, most importantly, undoped MPB BSPT possesses a higher T_C (≈ 450 °C at $x = 0.64$) which makes BSPT a promising material for use in the range 200–350 °C. Given the properties of BSPT piezoelectric ceramics, there is great potential for its usage in PTs designed to operate at higher temperatures than those based on PZT.

The objective of the work presented here is to demonstrate the effectiveness of BSPT as a material for high-temperature PTs for use in resonant power supplies. Additionally, the work will compare the performance of BSPT to state-of-the-art PZT ceramics and prove the effectiveness of PT-based resonant converters for high-temperature applications requiring up to 1 W in power. To achieve this, sample BSPT- and PZT-based PTs are fabricated and characterized using a variety of metrics at several temperatures, to evaluate the performance of BSPT compared to the current optimum PZT compositions when applied to PT applications.

2. PTs in Power Converters

2.1. PT Topology

Although the choice of PT topology is important for specific applications, when comparing two materials the PT topology choice will have a minimal impact on the results.

The ring-dot type PT, **Figure 1**, was chosen as the basis for this study since it is one of the simplest topologies to construct, requiring only a single piezoelectric disc, no bonding/glue, and a minimal number of electrodes. Its simple construction makes it relatively straightforward to produce two similarly dimensioned devices from different piezoelectric materials thereby allowing a fair comparison. The performance differences between PTs made of different materials, therefore, predominantly arise because of the materials alone. Ring-dot PTs are versatile, they can be used in both step-up or step-down applications;

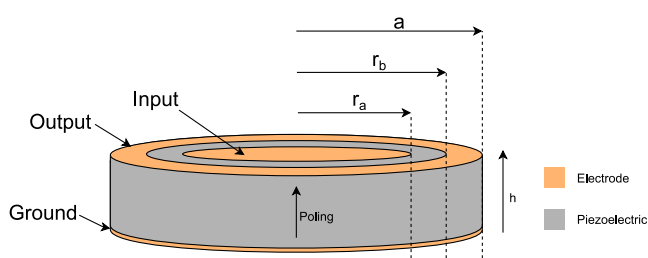


Figure 1. Ring-dot piezoelectric transformer (PT).

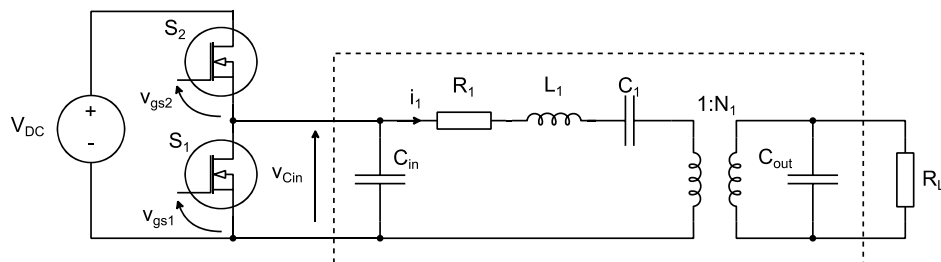


Figure 2. Inductorless half-bridge resonant inverter, the dashed region highlights the Mason equivalent circuit of the PTs.

they exhibit high power densities and show minimal spurious vibration modes.^[20,21]

Owing to the electromechanical nature of PTs, it is common for electrical engineers to approximate the PT using an equivalent circuit, namely the Mason equivalent circuit shown inside the dashed box in **Figure 2**. The input and output capacitance (C_{in} , C_{out}), model the physical plate capacitances generated between the input and output electrodes (located on the upper face in **Figure 1**), and the common ground electrode (located on the lower face). The ideal transformer ($1:N_1$) models the conversion between electrical and mechanical energy. Finally, the resistor–inductor–capacitor tank circuit models the mechanical resonance of the PT, with a resonant frequency $\omega_0 = 1/\sqrt{L_1 C_1}$ and R_1 representing the losses.

2.2. PT-Based Resonant Converters

Resonant power conversion is one of the most popular applications of PTs. Resonant converters rely on energy oscillating between parts of a “resonant tank,” traditionally constructed using discrete capacitors and inductors, which results in a sinusoidal current being generated. Resonant converters have displaced traditional “hard-switched” non-resonant electronic power converters in many applications because their continuously varying current allows semiconductor switches to be activated at instants of zero voltage or zero current, dramatically reducing switching energy losses and thereby increasing efficiency.

Due to their natural vibration modes, PTs can provide the “resonant tank” for such a converter. While several topologies of PT-based resonant converter have been studied, the choice of topology is typically related to a specific application and will have minimal impact on the performance comparison between PTs. Therefore, we relate our work only to the popular inductorless half-bridge inverter topology,^[22] as shown in **Figure 2**.

The half-bridge inverter uses two high-frequency metal-oxide–semiconductor field-effect transistor (MOSFET) switches, S_1 and S_2 , which operate at a frequency close to the resonant frequency of the piezoelectric transformer, as shown in **Figure 3**. Correct operation results in a high-frequency trapezoidal waveform at the input to the PT ($v_{C_{in}}$). Due to the high Q factor bandpass filter characteristic of the PT, the resonant current is approximately sinusoidal, as is the output voltage. It should also be noted that the current through the resonant circuit i_1 is proportional to the vibration velocity of the PT and $v_{C_{in}}$ is proportional to the electric field across the device. A full description of the operation of this converter can be found in ref. [22,23]

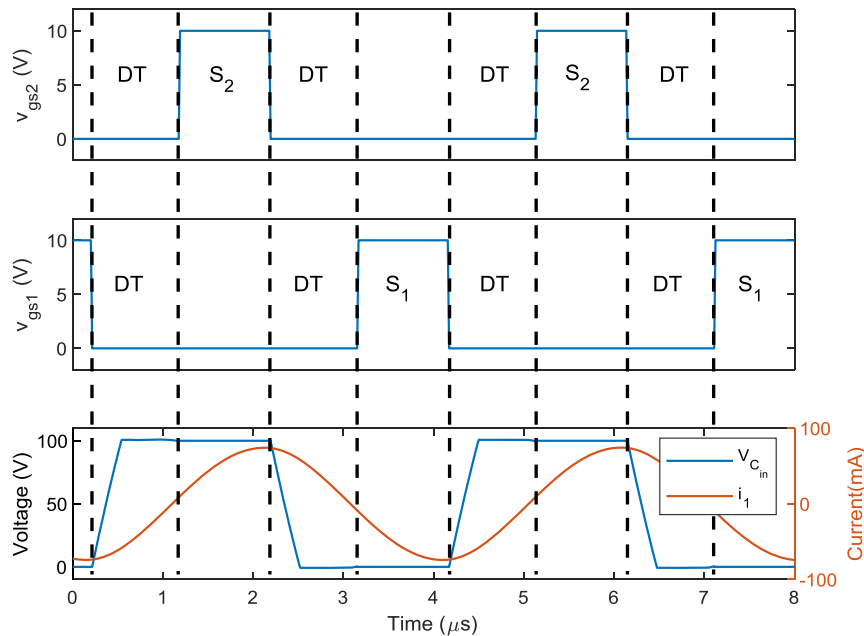


Figure 3. Input capacitor voltage, resonant current, and gate-source control signals for MOSFETs S_1 and S_2 in inductorless half-bridge resonant converter (where DT is the deadtime interval).

2.3. Power Converter Performance Metrics

2.3.1. k_{ZVS}

One of the main advantages of resonant converters is that they allow zero-voltage switching (ZVS) to be achieved, avoiding switching loss in the MOSFETs. During the deadtime interval (shown as DT in Figure 3) resonant current i_1 charges or discharges the input capacitor so that, at the point of turn-on, there is zero voltage across the relevant MOSFET. When ZVS is not achieved, C_{in} charges or discharges quickly through the switch causing energy loss. To evaluate the zero-voltage switching performance of the converter, k_{ZVS} is introduced

$$k_{ZVS} = \frac{v_{C_{in}} (@S_2 \text{ turn on})}{V_{DC}} \quad (1)$$

where ZVS is achieved if $v_{C_{in}} (@S_2 \text{ turn on}) \geq V_{DC}$, in which case $k_{ZVS} \geq 1$. When $k_{ZVS} < 1$, the switching losses in the MOSFETs are proportional to $(1 - k_{ZVS})^2$. If the PT is designed correctly and the switching waveforms displayed in Figure 3 are achieved, ZVS should be guaranteed.^[23]

2.3.2. Electrical Efficiency

A key performance metric for all power converters is electrical efficiency, defined as

$$\eta = \frac{\Re(P_{out})}{\Re(P_{in})} = \frac{\Re(P_{out})}{\Re(P_{out} + P_{loss})} \quad (2)$$

where P_{out} is the power delivered to the load, P_{in} is the input power to the converter, and P_{loss} is the power loss in the converter, mainly consisting of switching and conduction losses

in the MOSFETs and losses in the PT. Ideally, the efficiency of the converter should be maximized and thus losses are minimized. As discussed, with the appropriate design of the PT and control circuitry, ZVS is achieved, and thus switching losses can be avoided. Therefore, the electrical efficiency of an inverter is directly related to the losses in each PT during operation and is proportional to resistance R_1 (and thus the quality factor) in the Mason equivalent circuit (assuming MOSFET conduction loss is much smaller than PT loss).

2.3.3. Output Power

Output power is a key consideration when designing a converter, as it informs several of the design choices. In PT-based power converters, the output power of the converter is typically limited by the temperature rise, with a 30 °C rise in temperature over ambient being a typical limit.^[24] Some work has been done to model the effects of ambient temperature on temperature rise for other PT topologies,^[25] however, there is no available metric to determine the power limit of a PT at raised ambient temperatures and developing such as metric is beyond the scope of this work. As a result, we use output power to give context to the efficiency values that are achieved ensuring the results of the study are representative of a real-world application.

3. Experimental Procedure

3.1. PT Design

Figure 1 shows the design of a ring-dot PT with a ring and a dot electrode on the upper side and a full electrode on the lower side. The dimensions are as follows: radius $a = 8$ mm, thickness

$h = 1.1$ mm, $r_a = 3.4$ mm and $r_b = 6$ mm. The radius and thickness were selected to achieve a radius/thickness ratio of ≈ 7 , ensuring that the PT avoids interaction with spurious vibration modes,^[26] even though, as Erhart suggests, these modes are not excited in this PT topology.^[21] Second, r_a and r_b were chosen to achieve a capacitance ratio ($C_N = C_{in}/(N_1^2 C_{out})$) of less than $2/\pi$, to agree with the criterion presented by Foster et al.^[23] This ensures that an inductorless half-bridge power inverter constructed with this PT should achieve ZVS irrespective of the load (if the driving conditions presented in ref. [23] are adhered to). Identically dimensioned PTs based on this design were fabricated from both BSPT and PZT materials.

3.2. Ceramic Preparation

0.64(PbTiO₃)-0.36(BiScO₃) (BSPT-64) ceramics were prepared by the conventional solid-state route using PbO (99%, Sigma-Aldrich), Bi₂O₃ (99.9%, Sigma-Aldrich), Sc₂O₃ (99%, Sigma-Aldrich), and TiO₂ (99.9%, Sigma-Aldrich) as raw materials. Raw materials were pre-dried (300 °C for PbO, Bi₂O₃ and 800 °C for Sc₂O₃, TiO₂) for 8 h before weighing then ball-milled in isopropanol with yttria-stabilized zirconia milling media for 6 h. The mixture was then calcined twice at 800 and 900 °C followed by drying and sieving. Green pellets were formed using a uniaxial steel die and then cold-isostatically pressed at 200 MPa. Throughout this article, the term pellet was used to refer to the PT disc with or without full-face electrodes, and the term PT refers to a poled disc with the ring-dot electrodes. Pellets were sintered at 1200 °C for 2 h in a closed environment. During sintering, green pellets were buried in calcined powder of the same composition to minimize volatilization.

Pb(Zr,Ti)O₃ (PZT-P85) ceramics were prepared from commercial powder (P85, Weifang Jude Electron). Green pellets were formed using a uniaxial press and then cold-isostatically pressed under the same conditions as BSPT. Pellets of PZT-P85 were sintered at 1250 °C for 2 h in a closed environment with sacrificial powder to minimize volatilization.

3.3. X-Ray Diffraction and Scanning Electron Microscopy

The X-ray powder diffraction (XRD) analysis was performed on a high-resolution STOE STADI-P diffractometer (Cu K α emitter, STOE & Cie GmbH) using sintered and crushed samples. Microstructure and elemental compositions were determined by scanning electron microscope (SEM, Philips XL 30S FEG) and energy-dispersive X-Ray spectroscopy (EDX, Oxford Link ISIS) on polished surface/fracture surfaces of bulk ceramics.

3.4. Electrical Measurements of Material

Impedance spectroscopy and relative permittivity measurements were performed using either a Solartron Modulab or Hewlett Packard 4284A precision inductor–capacitor–resistor (LCR) meter. Au-paste electrodes were coated on the upper and lower faces of the pellets. Results were corrected for sample geometry (thickness/area) and high-frequency data was corrected for instrument error. For ferroelectric polarization-field (P-E) measurements, ceramics were ground to a thickness of ≈ 1 mm and

gold-sputtered. Bipolar P-E loops were obtained using an aixACCT TF 2000E ferroelectric tester at 1 Hz.

3.5. Fabrication of PTs

BSPT-64 and PZT-P85 pellets were coated at room temperature with an Ag electrode and poled for 30 mins at 40 kV cm⁻¹ at 120 °C. The Ag electrode was removed and the Au ring-dot/full electrode was sputtered onto both sides to form the PT samples, as shown in Figure 4.

3.6. PT Testing and Equivalent Circuit

An Elite tube furnace was used to vary the ambient temperature of the PT samples, from 25 to 200 °C for PZT-P85 samples and up to 250 °C for BSPT-64 samples. Each PT was suspended from a ceramic rod, allowing it to freely vibrate whilst in the furnace. An n-type thermocouple was placed ≈ 1 cm away from the PT and the temperature was logged 4 times per second using a Pico TC-08 datalogger. The temperature was adjusted, and the transient was allowed to settle until no change in temperature was observed for at least 20 min, before any small- or large-signal measurement was taken.

3.6.1. Small-Signal—Impedance Testing

The small-signal input impedance, Z_{in} , of each PT was measured using a 1 V excitation from an Omicron Bode 100 vector network analyzer. The output electrode of the PT is short-circuited to the ground electrode, and the impedance between the input electrode and ground electrode is measured. Similarly, the small-signal output impedance, Z_{out} , was measured between the output electrode and ground electrode, with the input electrode shorted to the ground electrode. Each impedance measurement was performed over a range of frequencies around the radial resonant frequency. From these measurements, the equivalent circuit components of the PT, shown in the Mason equivalent circuit (Figure 2) are extracted using a high damping component extraction method presented by Forrester et al.^[27]

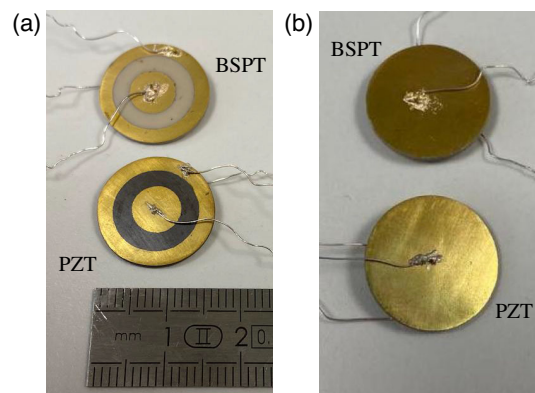


Figure 4. Image of sample ring-dot piezoelectric transformers, a) Upper face of (top) BSPT-64 and PZT-P85 (bottom) PT and b) Lower face of (top) BSPT-64 and PZT-P85 (bottom) PT.

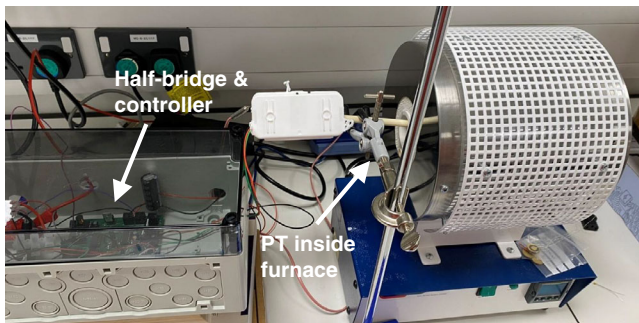


Figure 5. Testing setup for large signal measurements.

3.6.2. Large-Signal—Power Converter Testing

Efficiency and power measurements of each converter are taken using a Yokogawa PX8000 power oscilloscope. The input power is measured across the V_{DC} supply to the converter and the output power is measured across the R_L load resistance. From these measurements, the PX8000 calculates the overall electrical efficiency of each converter. An image of this measurement setup is shown in **Figure 5**.

The power electronic converter was operated with an 80 V DC input and a dedicated ZVS controller, based on the frequency doubler phased-locked loop control system described in ref. [22], which ensures the converter is operated at the correct frequency. By automatically adjusting the frequency, this controller ensures that the switch S_1 turns off at the zero-crossing of i_1 thereby allowing the greatest opportunity for i_1 to charge the voltage on capacitor C_{in} from 0 to 80 V before switch S_2 turns on after $\pi/2$ radians. In this way, ZVS is achieved.

To ensure a fair comparison between PT samples, the load resistance is matched to the output capacitor impedance. This “matched load” maximizes power transfer and can be calculated using^[28]

$$R_{L_{\text{matched}}} = \frac{1}{\omega C_{\text{out}}} \quad (3)$$

where ω is the angular switching frequency. The PT parameters including C_{out} are temperature-dependent and thus both the

operating frequency and matched load change with frequency. It is, therefore, impractical to use the exact matched load at each temperature step. Therefore, the measurement for each temperature was repeated for each of the load resistors 220 Ω , 500 Ω , and 1 k Ω . Values for the matched load, which depend on temperature, vary from 450 to 950 Ω . Results will be presented for the most efficient load, which is normally the load closest to the matched load at that temperature.

4. Results

4.1. Material Properties

The room temperature XRD patterns of sintered and crushed BSPT-64 and PZT-P85 pellets are shown in **Figure 6**. The presence of rhombohedral and tetragonal phases (the encircled 200 peak is split into three peaks in each pattern), characteristic of MPB compositions, were observed in the XRD patterns with no secondary phase peaks. A backscattered electron SEM image of a polished sample of BSPT-64 showed a homogeneous surface with no secondary phases present, **Figure 7a**, consistent with the XRD data. Fracture surfaces reveal a grain size of 3–5 μm and 1–2 μm for BSPT-64 and PZT-P85, respectively, **Figure 7b,c**.

The relative permittivity (ϵ_r) and dielectric loss ($\tan \delta$) of BSPT-64 and PZT-P85 are shown in **Figure 8**. ϵ_r of BSPT-64 and PZT-P85 are both $\cong 950$ at RT. The maximum value of ϵ_r ($\epsilon_{r,\text{max}}$) is $\cong 12\,000$ at $\cong 340^\circ\text{C}$ and 31 000 at $\cong 430^\circ\text{C}$ for PZT-P85 and BSPT-64, respectively. $\epsilon_{r,\text{max}}$ gives the approximate temperature of the phase transition to the paraelectric cubic phase and represents the point of depolarization at zero field. $\tan \delta$ is less than 0.1 for both samples below 400 $^\circ\text{C}$, but then increases steeply with increasing temperature for PZT-P85. In contrast, $\tan \delta$ of BSPT-64 only exceeds 0.1 above $\cong 630^\circ\text{C}$. ϵ_r under high voltage (5 kV) and low frequency (1 Hz) is also calculated at 5 kV cm^{-1} where both BSPT-64 and PZT-P85 possess a linear capacitor response. The results are higher compared to those obtained at low voltage and high frequency using an LCR meter, **Figure 8b**.

The bipolar polarization and strain hysteresis of BSPT-64 and PZT-P85 ceramics were measured at 120 $^\circ\text{C}$ under an electric field of 1 Hz and 40 kV cm^{-1} , **Figure 9**. The coercive fields

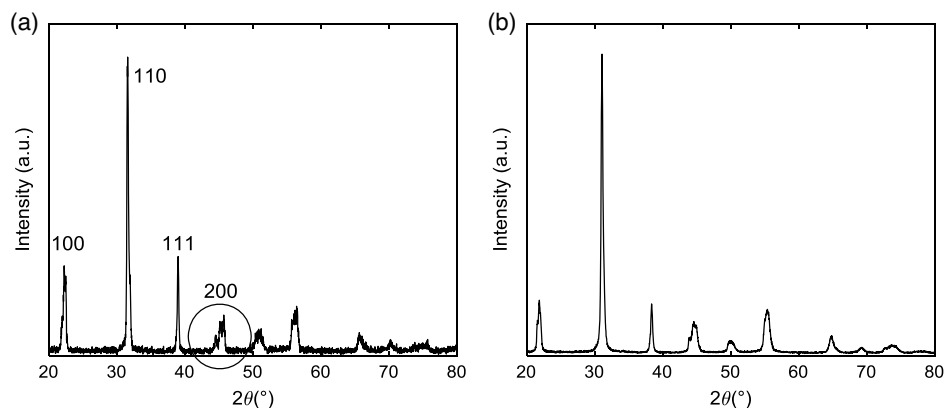


Figure 6. Room-temperature XRD data for: a) BSPT-64 and b) PZT-P85 ceramics. Major pseudocubic peaks are indexed and 200 peak is encircled to indicate the presence of R and T phases, typical of MPB compositions.

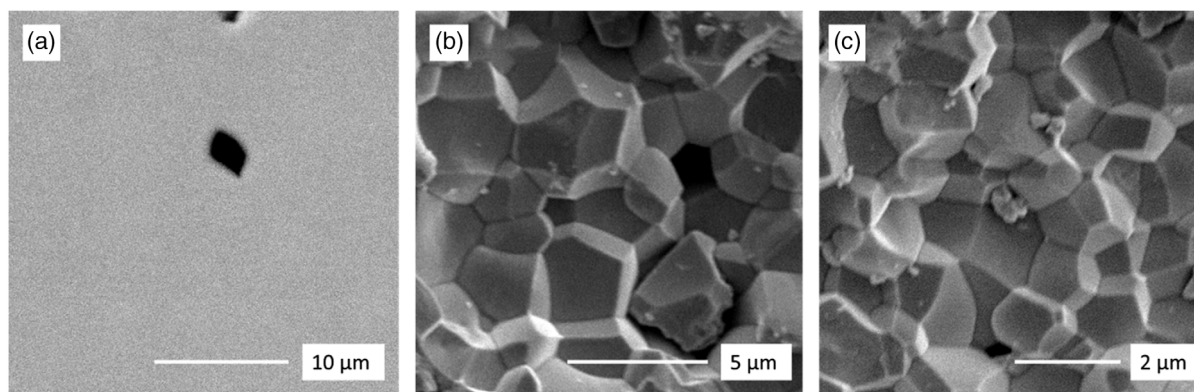


Figure 7. a) Back-scattered electron images for BSPT. Secondary electron images on a fracture surface of: b) BSPT-64 and c) PZT-P85.

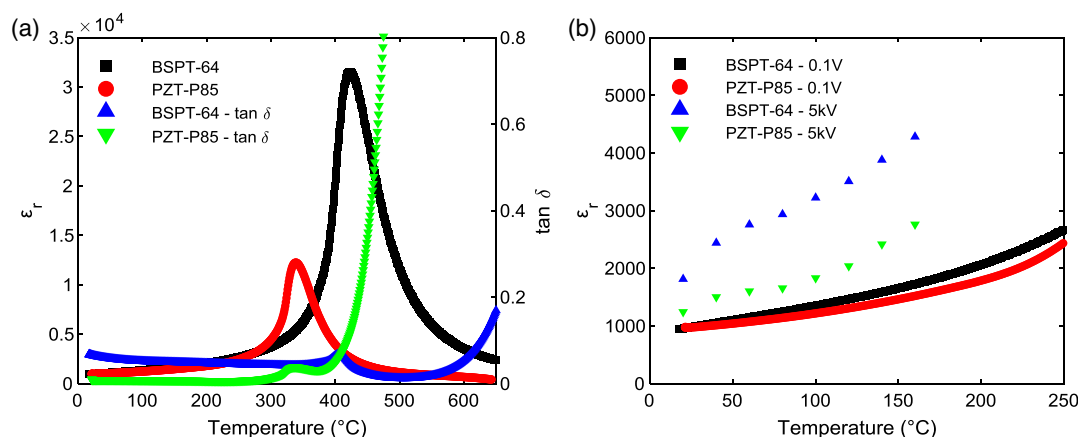


Figure 8. a) Temperature dependence of ϵ_r and $\tan \delta$ for BSPT-64 and PZT-P85 and b) ϵ_r of BSPT-64 and PZT-P85 measured under different voltages.

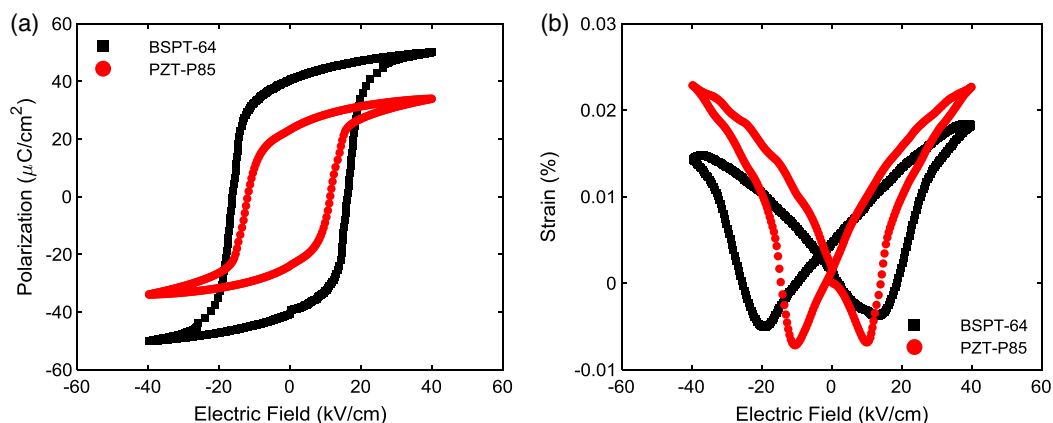


Figure 9. a) Polarization-electric field hysteresis curves and b) bipolar strain-electric field curves obtained at 120 °C for sintered pellets of BSPT-64 and PZT-P85 at a frequency of 1 Hz.

(E_C) and remnant polarizations (P_r) were $\cong 17 \text{ kV cm}^{-1}$ and $40 \mu\text{C cm}^{-2}$ for BSPT-64 and $\cong 12 \text{ kV cm}^{-1}$ and $23 \mu\text{C cm}^{-2}$ for PZT-P85, respectively. The bi-polar strain is higher in PZT-P85 ($\cong 0.23\%$) compared to BSPT-64 ($\cong 0.18\%$) at 120 °C.

A complex impedance plane (Z^*) plot for BSPT-64 and PZT-P85 at 450 °C is shown in Figure 10a. Both samples consist

of a single arc from ≈ 250 to 900 °C. To a first approximation, the arc could be modeled with a single parallel resistor-capacitor (RC) element as shown in Figure 10b inset. The associated capacitance for the arc is 80 pF cm^{-1} for BSPT-64 and 90 pF cm^{-1} for PZT-P85. These are consistent with values obtained from LCR measurements, thereby confirming them to be a bulk response.

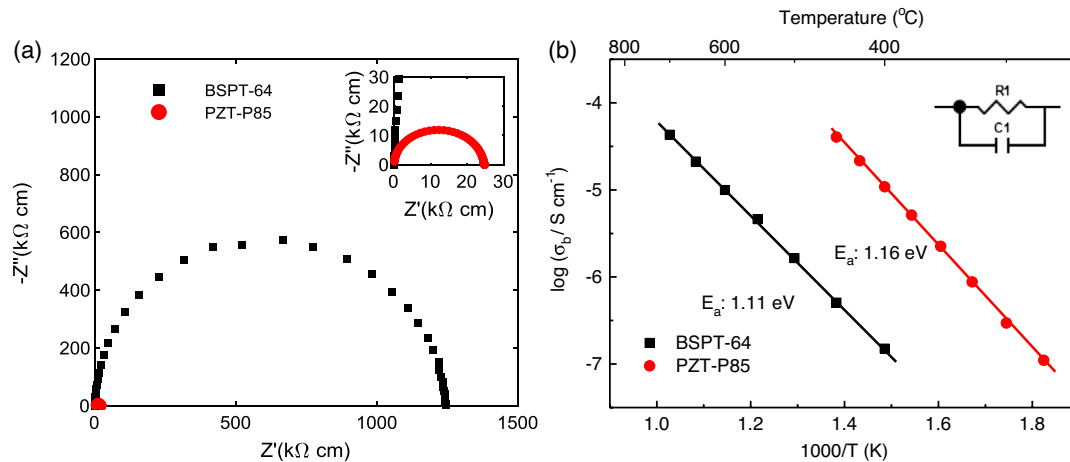


Figure 10. a) Z^* plots of BSPT-64 and PZT-P85 ceramics at 450 °C. b) Arrhenius plots of bulk conductivity as $\log \sigma_b$, versus reciprocal temperature for BSPT-64 and PZT-P85 ceramics.

The temperature dependence of the bulk (grain) resistance, R_b , was extracted from Z^* plots for both samples and summarized in an Arrhenius plot of the bulk conductivity, σ_b , where $\sigma_b = 1/R_b$, Figure 10b. The difference in σ_b between BSPT-64 and PZT-P85 is around 2 orders of magnitude whereas the activation energy, E_a , associated with the bulk conductivity is similar, 1.16 eV for PZT-P85 and 1.11 eV for BSPT-64.

4.2. Small-Signal Impedance Measurements

The loss (R_1) and Q factor extracted for both BSPT-64 and PZT-P85 PTs are shown in Figure 11a,b, respectively. Damping resistance of the PZT-P85 PT increased from 15 Ω at room temperature to 35 Ω at 200 °C, with a peak of 61 Ω at 100 °C. Conversely, the BSPT-64 PT exhibited a decrease in R_1 from 380 Ω at room temperature to 82 Ω at 250 °C. The Q-factor of the PZT-P85 PT decreased from 909 to 220 and the Q-factor of the BSPT-64 PT increased from 35 to 68 over the temperature range tested. For both PZT and BSPT, the ratio $QR_1 = \sqrt{L_1/C_1}$

decreases by a factor of about 2 over the studied temperature range, which by itself will suggest that the Q factor decreases with temperature. R_1 follows a different trend for each material. For BSPT, it changes roughly linearly by a factor of about 6, whereas for PZT it peaks before reducing. In both cases, it is the trend in R_1 that dominates the trend in Q factor.

The input (C_{in}) and output (C_{out}) capacitances extracted from both BSPT-64 and PZT-P85 PTs are shown in Figure 12, normalized to their room temperature value. Both PTs exhibit increases in both capacitances with temperature, agreeing with the ϵ_r results presented in Figure 8b. The capacitances of the BSPT-64 PT increased by a factor of 1.82 and the capacitances of the PZT-P85 PT increased by a factor of 1.39 across the range of temperatures. The larger increase in capacitance of BSPT-64 compared to PZT-P85, also agrees with the ϵ_r measurements shown in Figure 8b.

The resonant frequencies extracted from both BSPT-64 and PZT-P85 PTs are shown in Figure 13. The resonant frequency of the BSPT-64 PT decreases from 134.2 to 123.7 kHz, a decrease of 10.5 kHz across the temperature range. Conversely, the resonant frequency of the PZT-P85 PT increases from 136.6

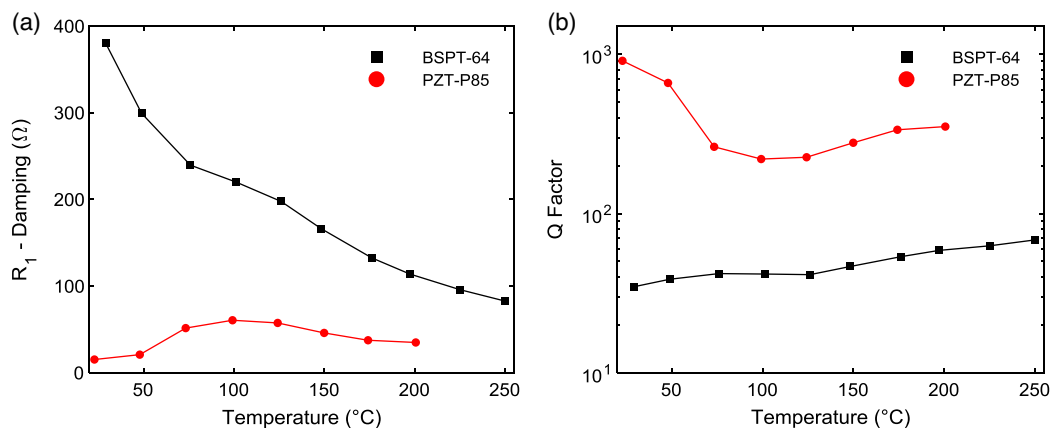


Figure 11. a) Damping resistance and b) Q factor of BSPT-64 and PZT-P85 PTs versus temperature.

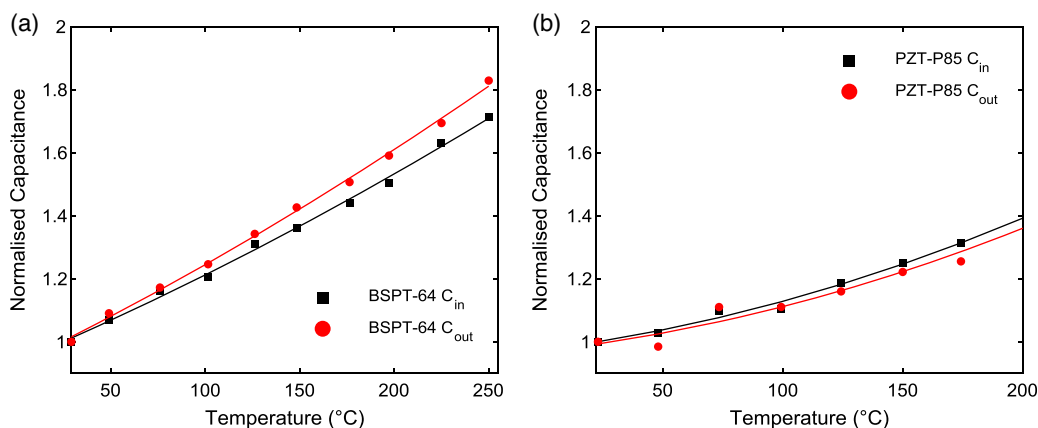


Figure 12. Normalized input and output capacitance versus temperature for: a) BSPT-64 and b) PZT-P85 PTs.

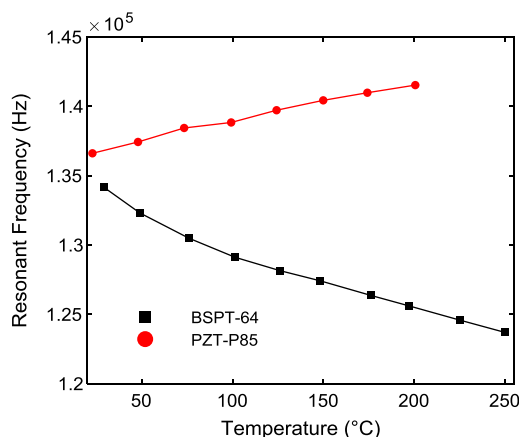


Figure 13. Resonant frequency versus temperature for both BSPT-64 and PZT-P85 PTs.

to 141.5 kHz, a 4.9 kHz increase across the temperature range, less than half that exhibited by the BSPT-64 PT.

4.3. Large-Signal Power Converter Measurements

4.3.1. Efficiency and Power

The efficiency and output power achieved by both BSPT-64 and PZT-P85 PT-based inductorless half-bridge inverters (section 0) driven at the correct frequency, with an 80 V input voltage and when driving the most efficient load, are shown in **Figure 14**.

The PZT-P85-based inverter achieves between 25.5 and 43.7 percentage points greater efficiency than the BSPT-64-based inverter across the 25–200 °C temperature range. The PZT-P85 sample achieves this higher efficiency at between 0.15 and 0.47 W greater output power than the BSPT-64-based inverter. This increase in efficiency in the PZT-P85-based inverter can primarily be attributed to the significantly lower damping resistance R_1 exhibited by the PZT-P85 PT. Whereas, with the PZT-P85 PT, efficiency degrades with temperature, the efficiency of the BSPT-64 based inverter increases by 15.3 percentage points across the full range of temperatures tested, while also exhibiting a 0.49 W increase in output power.

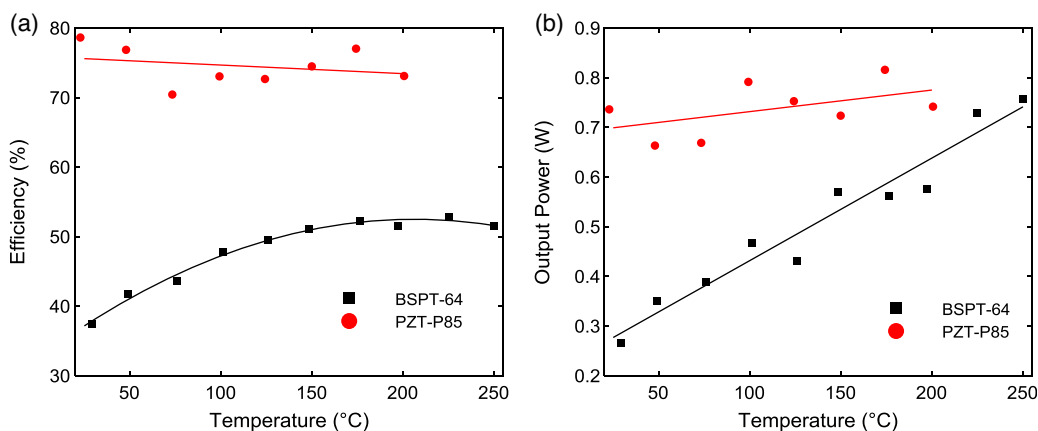


Figure 14. a) Efficiency and b) output power measurements versus temperature for both BSPT-64 and PZT-P85 inverters.

4.3.2. ZVS Factor k_{ZVS}

The $v_{C_{in}}$ voltage at the input to each PT during operation with a $500\ \Omega$ load is shown in **Figure 15**. As shown in Figure 15b, the voltage at the input to the PZT-P85 PT reaches V_{DC} before the high side MOSFET, S_2 , turns on at all temperature steps. Therefore, the PZT-based inverter achieves $k_{ZVS} \geq 1$ and thus achieves ZVS across the temperature range. In contrast, Figure 15a shows the voltage at the input to the BSPT-64 PT doesn't reach V_{DC} before S_2 turns on for temperature $< 200\ ^\circ\text{C}$. Therefore, ZVS ($k_{ZVS} \geq 1$) is only achieved by the BSPT-64 PT for temperatures $> 200\ ^\circ\text{C}$, thus this has some impact on the efficiency of the BSPT-64-based inverter at low temperatures as shown in Figure 14.

5. Discussion

The testing performed here shows that a PT made from BSPT-64 can be effectively used in a power converter and validates the performance of BSPT-64 PTs at temperatures up to $250\ ^\circ\text{C}$. Inverters made with BSPT-64 PTs show both improved output power and efficiency at elevated temperatures when compared to room temperature, mainly due to a reduction in the damping resistance R_1 and thus a reduction in the losses in this PT. However, PZT-P85 PTs clearly outperform the BSPT PTs in this application at temperatures less than $200\ ^\circ\text{C}$. This is primarily due to the low damping these PTs exhibit, giving rise to lower losses and better ZVS performance.

BSPT-64 PTs have one clear advantage over PZT-P85 PTs, as the Curie temperature of BSPT-64 is around $100\ ^\circ\text{C}$ higher than PZT-P85, thus allowing them to be used at temperatures greater than $200\ ^\circ\text{C}$ without depoling. Therefore, for temperatures up to $250\ ^\circ\text{C}$, unlike PZT-P85, BSPT-64 can successfully operate and with only a 25% performance degradation compared to PZT-P85 at $200\ ^\circ\text{C}$. Since the operating temperature of many magnetic components is limited to $100\ ^\circ\text{C}$, the higher temperature range of BSPT could translate to PT power supplies finding application in industries such as aerospace or oil, where temperatures in the range of $200\text{--}300\ ^\circ\text{C}$ are common. However, they would need to be used with high-temperature electronic devices, such as silicon carbide, which are also an area of intense research.^[29]

The BSPT PT properties show improvement with increasing temperature. Therefore, at temperatures greater than $250\ ^\circ\text{C}$ it is likely that BSPT-64 converter would achieve higher powers with similar levels of efficiency. The BSPT-64 PT-based converter presented here achieves around 60% efficiency at just under $0.7\ \text{W}$ output power at $250\ ^\circ\text{C}$, achieving results similar to high-temperature power supplies presented in the literature, while being much simpler to implement.^[30]

Observing the large efficiency differences between the PZT-P85 and BSPT-64 inverters, it is clear the PT is responsible for most of the losses, due to the relatively high damping resistance of the BSPT-64 PT. This larger damping resistance causes increased I^2R losses compared to the PZT-P85 PT and additionally, the larger output capacitance of the BSPT-64 PT also causes higher increases in resonant current, thus increases in I^2R losses. These issues can be attributed to the low Q factor (≈ 50) and the rapid increase in permittivity with temperature exhibited by the BSPT-64 material. Further improvements to the BSPT material to improve on these characteristics, would lead to significant performance improvements.

Another factor in the increased efficiency observed in the PZT-P85 inverter compared to the BSPT-64 PT is the improvement in k_{ZVS} . Whereas the PZT-P85 inverter achieves ZVS across the temperature range, BSPT-64 does not achieve ZVS at low temperatures. As Foster et al discuss, ZVS should always be achieved when $C_{in}/(N_1^2 C_{out}) < 2/\pi$, assuming 100% efficiency.^[23] However, at low temperatures, this relation no longer holds as the BSPT-64 PT's efficiency is significantly lower than 100%, owing to the large I^2R losses. The results presented in Figure 11 for BSPT-64 show that R_1 decreases with temperature providing a significant improvement in PT efficiency by helping to reduce the I^2R losses. Therefore, with increased temperature, k_{ZVS} increases, where at temperatures greater than $200\ ^\circ\text{C}$, $k_{ZVS} \geq 1$ and ZVS is achieved. If improvements to the design were made to either reduce the damping resistance or to lower the $C_{in}/N_1^2 C_{out}$ ratio, improved inverter efficiency at lower temperatures could be achieved.

It should be noted that traditional silicon-based components were used for the additional circuitry in the experimental work and as these components cannot perform at high temperatures

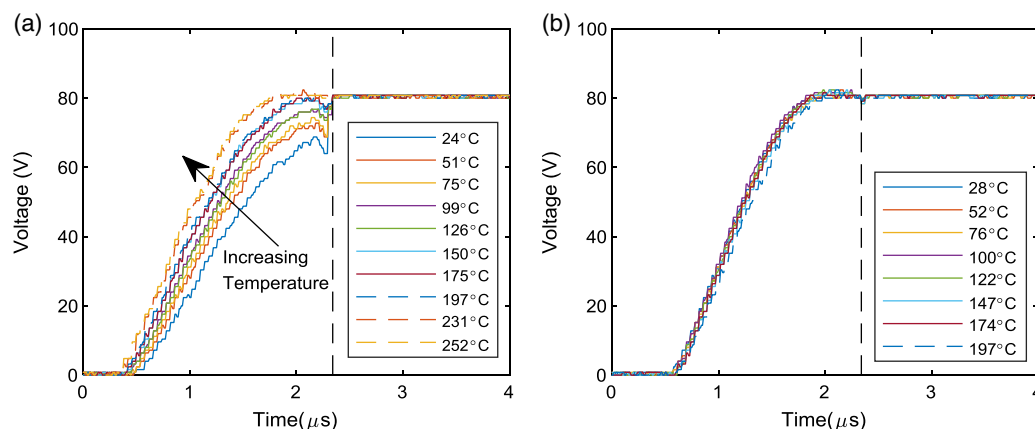


Figure 15. $v_{C_{in}}$ voltage waveforms for: a) BSPT-64 inverter and b) PZT-P85 inverter, with a $500\ \Omega$ load. The dashed line indicates the point of S_2 turns on.

(>150 °C), only the PT was kept in the furnace during testing. Consequently, lengthy wires were used to connect the PT to the main circuitry ($\cong 30$ cm) and testing equipment ($\cong 100$ cm). This causes unwanted resonances and additional parasitic elements which likely affected the performance of both converters.

6. Conclusions

A suitability analysis for the use of BSPT-64 based PTs in high-temperature resonant power inverters is presented. A similar state-of-the-art PZT-P85-based PT is also fabricated for comparison. A detailed description of the design and fabrication of both samples is presented. XRD, SEM, impedance spectroscopy, and relative permittivity-temperature measurements on samples of the two materials are presented and discussed. Impedance analysis was performed on the resulting PTs allowing their equivalent circuit properties to be characterized. Finally, resonant inverters were constructed with both PTs, and power and efficiency measurements were taken at several temperatures. The results of this testing have shown that although the performance of the BSPT-64-based PT is not as good as the PZT-P85 PT, the BSPT-64 based PT performs effectively at temperatures well in excess of that possible to achieve with PZT-P85 and with comparable results to high-temperature traditional converters.

Acknowledgements

The authors thank the EPSRC for funding (FPeT: Framework for designing piezoelectric transformer power supplies, EP/P015859/1). For the purpose of open access, the author has applied a Creative Commons Attribution (CC BY) license to any Author Accepted Manuscript version arising.

Conflict of Interest

The authors declare no conflict of interest.

Data Availability Statement

The data that support the findings of this study are available from the corresponding author upon reasonable request.

Keywords

BSPT, high temperature, piezoelectric transformers, PZT, resonant power supplies

Received: April 21, 2022

Revised: July 26, 2022

Published online:

- [1] B. Jaffe, W. R. Cook, H. Jaffe, *Piezoelectric Ceramics*, Academic Press, Cambridge MA **1971**.
- [2] W. P. Mason, H. Baerwald, *Phys. Today* **1951**, 4, 23.
- [3] W. A. McCartney, *J. Inst. Electr. Eng.* **1960**, 6, 302.
- [4] T. Martinez, G. Pillonnet, F. Costa, *IEEE Trans. Power Electron.* **2018**, 33, 2241.
- [5] M. Ekhtiari, T. G. Zsurzsan, M. A. E. Andersen, Z. Zhang, *IEEE Trans. Power Electron.* **2018**, 33, 8101.
- [6] A. E. Crawford, *J. Br. Inst. Radio Eng.* **1961**, 21, 353.
- [7] F. Roccaforte, P. Fiorenza, G. Greco, R. Lo Nigro, F. Giannazzo, F. Iucolano, M. Saggio, *Microelectron. Eng.* **2018**, 187–188, 66.
- [8] R. R. Grzybowski, in *1998 High-Temperature Electronic Materials, Devices and Sensors Conf. (Cat. No.98EX132)*, San Diego, CA, USA **1998**, p. 172.
- [9] J. Colmenares, S. Kargarrazi, H. Elahipanah, H. Nee, C. Zetterling, in *2016 IEEE 4th Workshop on Wide Bandgap Power Devices and Applications (WiPDA)*, IEEE, Piscataway NJ **2016**, p. 271.
- [10] R. A. Normann, *First High-temperature Electronics Products Survey 2005*, United States **2006**, <https://doi.org/10.2172/889944>.
- [11] J. Watson, G. Castro, *J. Mater. Sci.: Mater. Electron.* **2015**, 26, 9226.
- [12] B. Jaffe, R. S. Roth, S. Marzullo, *J. Appl. Phys.* **1954**, 25, 809.
- [13] B. Jaffe, R. S. Roth, S. Marzullo, *J. Res. Natl. Bur. Stand.* **1955**, 55, 239.
- [14] Y. Yamashita, *Jpn. J. Appl. Phys.* **1994**, 33, 5328.
- [15] S. E. Park, T. R. Shrout, *IEEE Trans. Ultrason. Ferroelectr. Freq. Control* **1997**, 44, 1140.
- [16] R. E. Eitel, C. A. Randall, T. R. Shrout, P. W. Rehrig, W. Hackenberger, S.-E. Park, *Jpn. J. Appl. Phys.* **2001**, 40, 5999.
- [17] R. E. Eitel, C. A. Randall, T. R. Shrout, S.-E. Park, *Jpn. J. Appl. Phys.* **2002**, 41, 2099.
- [18] S. Zhang, C. A. Randall, T. R. Shrout, *Jpn. J. Appl. Phys.* **2004**, 43, 6199.
- [19] C. A. Randall, A. Kelnberger, G. Y. Yang, R. E. Eitel, T. R. Shrout, *J. Electroceram.* **2005**, 14, 177.
- [20] S. Priya, S. Ural, H. W. Kim, K. Uchino, T. Ezaki, *Jpn. J. Appl. Phys.* **2004**, 43, 3503.
- [21] J. Erhart, P. Pulpán, R. Dolecek, P. Psota, V. Lédl, *IEEE Trans. Ultrason. Ferroelectr. Freq. Control* **2013**, 60, 1612.
- [22] Z. Yang, J. Forrester, J. N. Davidson, M. P. Foster, D. A. Stone, *IEEE Trans. Power Electron.* **2020**, 35, 10466.
- [23] M. P. Foster, J. N. Davidson, E. L. Horsley, D. A. Stone, *IEEE Trans. Power Electron.* **2016**, 31, 5057.
- [24] E. L. Horsley, M. P. Foster, D. A. Stone, in *2007 European Conf. on Power Electronics and Applications*, Aalborg, Denmark **2007**.
- [25] J. Hu, *IEEE Trans. Ultrason. Ferroelectr. Freq. Control* **2003**, 50, 594.
- [26] J. Forrester, J. Davidson, M. Foster, in *PCIM Europe 2018; Int. Exhibition and Conf. for Power Electronics, Intelligent Motion, Renewable Energy and Energy Management*, Nuremberg, Germany **2018**, p. 1.
- [27] J. Forrester, L. Li, J. N. Davidson, M. P. Foster, D. A. Stone, D. C. Sinclair, I. M. Reaney, *Electronics Letters* **2020**, 56, 347.
- [28] G. Ivensky, I. Zafrany, S. Ben-Yaakov, *IEEE Trans. Power Electron.* **2002**, 17, 1049.
- [29] X. She, A. Q. Huang, Ó. Lucía, B. Ozpineci, *IEEE Trans. Ind. Electron.* **2017**, 64, 8193.
- [30] R. Perrin, N. Quentin, B. Allard, C. Martin, M. Ali, *IEEE J. Emerg. Sel. Top. Power Electron.* **2016**, 4, 1077.